



UNIVERSITÀ
DEGLI STUDI
DI UDINE

Università degli studi di Udine

Probing the influence of citrate-capped gold nanoparticles on an amyloidogenic protein

Original

Availability:

This version is available <http://hdl.handle.net/11390/1064235> since 2021-03-15T17:40:08Z

Publisher:

Published

DOI:10.1021/nn506161j

Terms of use:

The institutional repository of the University of Udine (<http://air.uniud.it>) is provided by ARIC services. The aim is to enable open access to all the world.

Publisher copyright

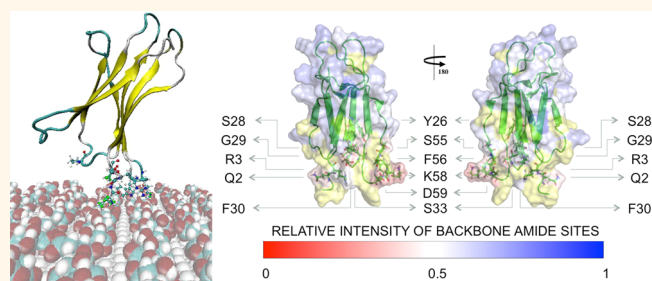
(Article begins on next page)

Probing the Influence of Citrate-Capped Gold Nanoparticles on an Amyloidogenic Protein

Giorgia Brancolini,^{*,†} Alessandra Corazza,^{*,§} Marco Vuano,[‡] Federico Fogolari,^{*,§} Maria Chiara Mimmi,[‡] Vittorio Bellotti,^{§,⊥,||} Monica Stoppini,^{§,⊥} Stefano Corni,^{*,†} and Gennaro Esposito^{*,‡,§,¶}

[†]Center S3, CNR Institute Nanoscience, Via Campi 213/A, 41125 Modena, Italy, [‡]Dipartimento di Scienza Mediche e Biologiche (DSMB), University of Udine, Piazzale Kolbe 3, 33100 Udine, Italy, [§]Istituto Nazionale Biostrutture e Biosistemi, Viale medaglie d'Oro 305, 00136 Roma, Italy, [⊥]Dipartimento di Medicina Molecolare, Universita' di Pavia, Via Taramelli 3, 27100 Pavia, Italy, ^{||}Division of Medicine, University College of London, London NW3 2PF, U.K., and [¶]Science and Math Division, New York University at Abu Dhabi, Abu Dhabi, UAE

ABSTRACT Nanoparticles (NPs) are known to exhibit distinct physical and chemical properties compared with the same materials in bulk form. NPs have been repeatedly reported to interact with proteins, and this interaction can be exploited to affect processes undergone by proteins, such as fibrillogenesis. Fibrillation is common to many proteins, and in living organisms, it causes tissue-specific or systemic amyloid diseases. The nature of NPs and their surface chemistry is crucial in assessing their affinity for proteins and their effects on them. Here we present the first detailed structural characterization and molecular mechanics model of the interaction between a fibrillogenic protein, β_2 -microglobulin, and a NP, 5 nm hydrophilic citrate-capped gold nanoparticles. NMR measurements and simulations at multiple levels (enhanced sampling molecular dynamics, Brownian dynamics, and Poisson–Boltzmann electrostatics) explain the origin of the observed protein perturbations mostly localized at the amino-terminal region. Experiments show that the protein–NP interaction is weak in the physiological-like, conditions and do not induce protein fibrillation. Simulations reproduce these findings and reveal instead the role of the citrate in destabilizing the lower pH protonated form of β_2 -microglobulin. The results offer possible strategies for controlling the desired effect of NPs on the conformational changes of the proteins, which have significant roles in the fibrillation process.



KEYWORDS: nanoparticles · amyloid · fibrillogenesis · docking · molecular dynamics · nuclear magnetic resonance

The interaction between proteins and nanoparticles (NPs)^{1–5} is central to many aspects of nanoscience and several nanotechnological applications.⁶ Among these, examples of relevant areas of interest are the nanoparticle-based medical imaging and drug delivery.^{7–10} These applications entail the administration of NPs to living organisms, which raises a number of issues concerning immunology, toxicology, biochemistry, biophysics, etc., often leading to assessment and analysis of NP/protein interaction processes that are central also in nanoscale bioanalytics.^{11,12} The subject of NP/protein interaction has been addressed by several investigators over the past decades, and recent reviews are available to summarize the state-of-the-art technology.^{4,13,14} From a general viewpoint, nanoparticles have been reported to

either affect or leave unchanged protein structure and function, depending on the specific properties of the nanoparticle surface and dimensions, the environmental conditions, and the actual protein characteristics.^{4,14,15} The basic pattern that proteins elicit on interaction with NPs is the formation of tightly and/or loosely bound layers around the NPs. These layers are referred to as corona and represent the very essence of the relationship between the NPs and the surrounding biological environment.¹⁶

Particular relevance has been attributed to the interaction of NPs with amyloidogenic proteins due to the interest in possible therapeutic approaches^{17–20} for a class of pathologies with poor treatment, if any. Most of the available evidence, however, points to an enhanced amyloid fibril formation

* Address correspondence to giorgia.brancolini@nano.cnr.it, stefano.corni@nano.cnr.it, gennaro.esposito@uniud.it.

Received for review October 29, 2014 and accepted February 19, 2015.

Published online 10.1021/nn506161j

© XXXX American Chemical Society

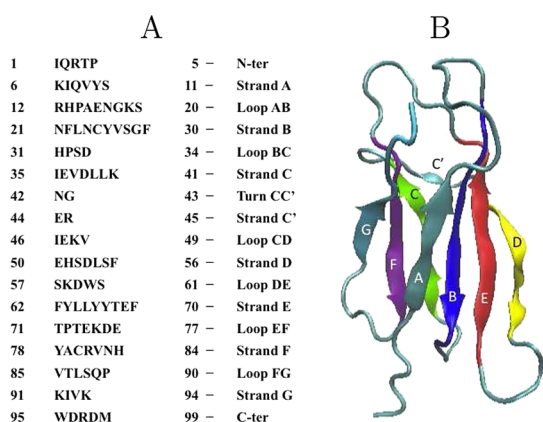


Figure 1. (A) Protein sequence. (B) Tertiary structure and topology of β_2 -microglobulin.

in the presence of NPs.^{19,20} In particular, it was shown²¹ that different types of NPs, such as copolymer particles, cerium oxide particles, quantum dots, and carbon nanotubes, enhance the fibril nucleation rate of β_2 -microglobulin (β_2 m), that is, the light chain of the class I major histocompatibility complex (MHC-I) that is responsible for a tissue-specific amyloidosis in long-term hemodialyzed patients.²² Secondary and tertiary structure and topology of β_2 m are reported in Figure 1.

As β_2 m fibrils did not appear physically linked to any of the NPs accelerating their onset, the faster growth was attributed to increased protein concentration in the vicinity of the NP surface, with a mechanism that had already been proposed to account for the protein tissue-specific deposition in collagen-rich regions.²³ However, a microscopic characterization of the β_2 m–NP interaction is still lacking, preventing a chemical understanding of the mechanisms that govern the fate of the protein. We present here a comprehensive investigation of β_2 m in the presence of citrate-coated gold NPs that, by combining synergically experiments and simulations, unravels such a microscopic picture. Citrate anions reduce gold ions to atoms and stabilize colloidal AuNPs formed from clustered atoms,²⁴ and the so-formed citrate-capped gold nanoparticles (cit-AuNPs) are among the most investigated in this field.^{3,25–28} Despite the large number of experimental investigations exploiting cit-AuNPs, the structural details of citrate anions adsorbed on the AuNP surface are still poorly understood.²⁹ Yet, they certainly constitute an array of negative charges that can interact with proteins. This is particularly relevant for β_2 m because, for its tissue-specific deposition, a mechanism has been proposed based on the effects of the collagen²³ and heparin³⁰ charge arrays in promoting local concentration increase and fibril nucleation.

To advance the understanding of the mechanisms driving the adsorption/deposition of amyloidogenic proteins to charged surfaces and the potential influence on fibrillogenesis, we present a comprehensive study based on the protein structural characterization

by NMR and molecular simulations of the protein/nanoparticle system. Both simulations and experimental results support the conclusions that cit-AuNPs, in the physiological-like experimental conditions probed here, have a quite labile interaction with β_2 m that does not lead to fibrillation. Our combined experimental and simulation approach reveals the protein patch interacting with the NP and suggests that conformational rearrangements associated with protein protonation are accentuated by the interaction with the citrate adlayer.

Not surprisingly, our findings on the NP effects on fibrillation are different from those previously obtained with other NPs and in other environmental conditions on this amyloidogenic protein. The previously reported results²¹ have been paradigmatic and rather influential for most of the successive interpretations, but, as pointed out in a commentary to the original report,³¹ different scenarios can be envisaged because of the enormous variability that is possible for the NP size, shape, surface coating, and composition. By learning how to exploit that variability, we aim at specifically fine-tuning the NP properties to rescue protein fibrillation or revert their amyloid deposition.¹⁸

RESULTS AND DISCUSSION

Docking of β_2 m on Negative Gold. In this section, we investigate the nature of the binding of β_2 m to a citrate-coated gold surface by means of Brownian dynamics (BD) docking.

Among the various crystal surfaces, we have considered the (111) plane (*i.e.*, Au(111)), which is the most stable and the most commonly occurring in nanoparticles.³² In this section, we shall consider extended gold surfaces, larger than the crystal faces that can be found on the experimental 5 nm gold NP. This simplifying assumption might create differences on the extent of the electrostatic interaction felt by the protein. The role of the finite particle size on the electrostatic interaction will be specifically tested by a continuum electrostatic model in the Role of Nanoparticle Actual Size on the Electrostatic Interaction section. Finally, for a surfactant-covered nanoparticle, possibly reactive edges and vertexes are certainly passivated by the surfactant itself.

The nature of the binding of β_2 m to a citrate-coated gold surface, as well as the effect of a negative surface potential, was initially investigated by introducing a small negative charge density per gold surface atom. The charge density of ($\text{Au}_{\text{chg}}^{\text{net}} = -0.05e$) per surface atom used in the calculation was determined by assuming an ordered monolayer of fully deprotonated citrate molecules on gold, as shown in Figure 2. The regular citrate adlayer on the top of Au(111) was generated with a ratio of the surface gold ion and citrate concentrations that was suitable to reproduce experimental electrochemical data on the cit-AuNP

system under aqueous conditions and at physiological pH.^{33,39}

In short, we generated the structures of protein–surface encounter complexes by running Brownian dynamics simulations during which the internal structure of the protein was kept rigid (rigid docking). The interaction (free) energy of the protein with the surface was obtained using the ProMetCS protein–metal continuum solvent model,⁴⁰ and adsorption free energies of β_2m on the Au(111) surface were computed for the structures resulting from the docking. The protein–surface encounter complexes obtained during a BD simulation trajectory were clustered to identify genuinely different protein orientations. For each of the most populated complexes, which were ranked by size, a representative structure was selected.

During docking, the interaction energy of the protein with the Au(111) surface is described by three main terms:⁴⁰ van der Waals energy described by site–site Lennard-Jones, E_{LJ} , interactions; adsorbate–metal electrostatic interaction energy, U_{EP} ; and the desolvation energy of the protein, U_{ds}^p , and of the metal surface, U_{ds}^m (see Table 1). The electrostatic term arises from surface polarization and includes an image-charge term.⁴¹

When this docking procedure was applied to the β_2m –AuNP system with negatively charged gold surface atoms ($Au_{chg}^{neg} = -0.05e$), it yielded a single orientation accounting for more than 98% of the total encounter complexes. The representative structure of the resulting complex is shown in Figure 3. The complex stability and the protein residues contacting the surface are listed in Figure 1.

The binding in complex A is stabilized mostly by the electrostatic terms. The preferred orientation involves

the residues at the N-terminal (ARG3) tail and DE loop (LYS58, ASP59, and TRP60). The strong and highly populated binding seems to be associated with the total charge of the gold surface atoms and the amount of charged residues contacting the surface (see Table 1), and this is due to the fact that in the presence of negatively charged gold the protein is able to use simultaneously more than one charged contact in order to optimize the binding. For completeness, we extended the docking to surfaces with 5-fold lower surface charge density ($Au_{chg}^{net} = -0.01e$). Complex A remains the most populated, but other complexes also appear (results are reported Figure 1 and Table 1 of Supporting Information).

Atomistic Molecular Dynamics (MD) Simulations of β_2m on Citrate-Covered Au. In order to disclose the possible conformational changes induced on the structure of the protein by the adsorption on cit–AuNPs, which may have significant roles in the fibrillation process, the stability of the encounter complexes resulting from the rigid docking was assessed by performing atomistic MD simulations.

As an atomistic molecular mechanics model for cit–AuNPs, we propose a surface in which the fully deprotonated citrate anions ($C_3H_5O(COO)_3^{3-}$) are described as interacting adsorbed species on a positively charged AuNP. For the sake of completeness, we also consider the comparison with a different citrate-covered surface model based on a neutral gold core and the

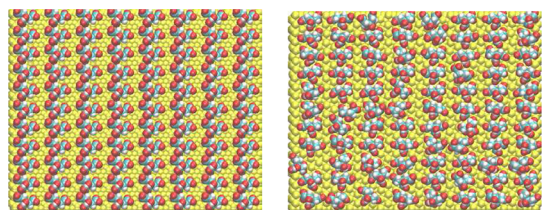


Figure 2. Initial (on the left) and final (on the right) citrate anion distribution on positively charged Au(111) after 20 ns of classical MD with GoIP and OPLS/AA in SPC/E water.

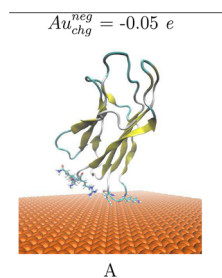


Figure 3. Most populated encounter complex of β_2m on a negatively charged gold nanocluster obtained by BD simulation. For $Au_{chg}^{neg} = -0.05e$, the structure of a single complex is representative for 98% of the total encounter complexes. The protein backbone is shown as cartoon representation. The residues contacting the gold surface are shown in stick representation.

TABLE 1. Resultant Encounter Complex from Rigid-Body BD Docking of β_2m (1JNJ) to a Au(111) Surface^a

label	RelPop % ^b	U_{Repr} ^c	E_{LJ} ^d	$E_{LJ} + U_{ds}^p + U_{ds}^m$ ^e	U_{EP} ^f	spread ^g	contact residues ^h
A	98	−41.380	−44.020	−10.278	−31.100	0.322	ARG3 LYS58 ASP59 TRP60

^a A hierarchical clustering algorithm (based on a minimum distance linkage function) was applied to the diffusional encounter complexes after docking to a bare negative gold ($Au_{chg}^{neg} = -0.05e$) surface. The reported complexes represent 98% of the encounter complexes obtained by BD simulation. ^b Relative population of this cluster. ^c U_{Repr} : Total interaction energy of the representative of the given cluster in kT with $T = 300$ K. ^d E_{LJ} : Lennard-Jones energy term for the representative complex. ^e U_{ds}^p : Nonpolar (hydrophobic) desolvation energy of the representative complex, in kT . ^f U_{ds}^m : Surface desolvation energy of the representative complex, in kT . ^g U_{EP} : Total electrostatic energy of the representative complex, in kT . ^h Root-mean-square deviation of the structures within the cluster with respect to the representative complex. ⁱ Residues with atoms contacting gold at distances ≤ 3 Å.

211 counterions included in aqueous solution over the
212 citrate, namely, cit3Na-AuNPs (*i.e.*, three Na^+ ions
213 released from each sodium citrate when it is put in
214 aqueous solution). Simulation results are summarized
215 in the Supporting Information (section Validation of
216 the Au surface with a positive charge density and
217 Figure 3). Such results are qualitatively similar to those
218 presented later in the main text for the positive gold
219 core model, although in somewhat less agreement with
220 NMR data in the main text model. In fact, we believe that
221 the choice of a positive gold core is more in line with
222 current understanding of citrate-covered gold nanopar-
223 ticles. For instance, in ref 33, the authors reported an
224 open circuit potential for freshly formed colloids
225 (460–560 mV vs SCE), corresponding to a positive gold
226 core for both pH 1 and pH 3 accompanied by a modest
227 tendency of the gold core to be pH-sensitive in passing
228 from pH 1 to pH 3. In our opinion, the latter results
229 support the assumption of a positive gold core even at
230 higher pH. More importantly, in ref 34, a positive gold NP
231 core at pH 7.5 was proposed on the basis of experi-
232 ments. Additionally, in ref 35, the authors reported a ζ -
233 potential of –40 to –50 mV for 10 nm nanoparticles, in a
234 pH range from 5 to 12. The ionic strength was not clearly
235 reported there, but it was reasonable to assume that it
236 was about 20–30 mM at neutral pH. Based on a
237 Poisson–Boltzmann estimate, this ζ -potential would
238 require a surface charge density of approximately
239 -0.2 e/nm^2 . Such values must be reproduced with a
240 citrate surface concentration, which in previous works
241 was reported to be in the range from 1.4×10^{-10} to $5 \times$
242 $10^{-10} \text{ mol/cm}^2$.^{36,37} Our atomistic model satisfies these
243 experimental constraints, by using a reasonable citrate
244 surface concentration of $2.8 \times 10^{-10} \text{ mol/cm}^2$ and by
245 including a positive gold core to obtain a surface charge
246 density of -0.3 e/nm^2 .

247 To our knowledge, the formation of a citrate ad-
248 sorption layer (adlayer) composed of interacting citrate
249 molecules as a stabilizing layer has never been incor-
250 porated in simulations due to the lack of suitable force
251 fields (FFs) able to describe the citrate anion, as well as
252 their interfacial physisorption on the top of the gold
253 nanoparticle. Such FFs were developed only recently.³⁸

254 At first, the stability of the citrate adlayer on the top
255 of Au(111) in aqueous solution was assessed by using
256 20 ns of standard MD simulations at 300 K. The initial
257 and final distributions of the citrate anion on the
258 positively charged AuNP are shown in Figure 2. None
259 of the citrate was displaced from the surface during
260 the entire length of the simulation in explicit water, in
261 line with experimental knowledge. The distribution of
262 citrate was stabilized on the top of the AuNP surface by
263 direct contact with the surface gold atoms, and no
264 large distortion of the adlayer from the initial confor-
265 mation has been observed.

266 In order to enhance the effective sampling space of
267 our protein–cit–AuNP system, we have applied REMD

involving multiple independent simulations at differ- 268
ent temperatures (T-REMD). In the present simulation 269
protocol, the system periodically attempts an ex- 270
change in temperature space,^{42,43} thus enabling repli- 271
cas at low temperature to exchange to a higher 272
temperature where energy barriers may be more easily 273
crossed. In this way, we overcome the limit of straight 274
MD simulations which are known to suffer from the 275
quasi-ergodic problem; that is, simulations at low 276
temperature tend to get trapped in a local minimum 277
energy state.⁴² 278

279 Given the experimental evidence demonstrating
280 that the neutral nonprotonated wild-type $\beta_2\text{m}$ does
281 not form amyloid fibrils *in vitro*,^{44–46} we have gener-
282 ated the effect of both nonprotonating and protonat-
283 ing conditions by using two fully solvated systems,
284 which were equilibrated under constant temperature
285 for 20 ns with standard MD: (i) nonprotonated normal
286 $\beta_2\text{m}$ (PDB code 1JNJ, *i.e.*, with only HIS51 and HIS84
287 protonated); (ii) protonated normal $\beta_2\text{m}$ (PDB code
288 1JNJ with also HIS31 protonated). The present experi-
289 mental pH conditions are correctly described by a
290 nonprotonated regime for the protein, but given the
291 presence of the negative citrate adlayer which may
292 stabilize the protonated regime, both regimes may be
293 relevant and should be investigated. The comparison
294 of the two protonation states is very important here
295 because the protonation state has been found to be
296 relevant in determining the stability of the protein and
297 of the barrier crossing energies between the normal
298 and amyloidogenic form of βm .^{47–51} For example, a
299 very low pH was used in ref 21, at which HIS31 is
300 certainly protonated.

301 Before starting the T-REMD, we applied to both
302 systems an equilibration protocol which consists of
303 various steps of optimization of atomic coordinates
304 and restrained finite-temperature dynamics during
305 which the restraints on protein atoms were gradually
306 weakened and eventually released, according to a
307 previously reported procedure.^{52–54} At the end of
308 the equilibration, the trajectories were stable in terms
309 of density, temperature, potential energy, and other
310 macroscopic properties. The equilibration phases of
311 the nonprotonated and protonated protein were fol-
312 lowed by 20 ns of unrestrained T-REMD in which 32
313 replicas on the top of the cit–Au(111) surface for each
314 system were used, yielding an aggregated simulation
315 time of 640 ns. During the 20 ns of T-REMD, the
316 proteins of each replica were fully flexible and the
317 water molecules, ions, and citrates were treated
318 explicitly in the simulations.

319 Simulation results are summarized in Figure 4 in
320 which panel (a) refers to nonprotonated protein and
321 panel (b) refers to protonated protein.

322 The top panel of Figure 4a shows the final repre-
323 sentative structures of the two most recurrent orien-
324 tations found for the nonprotonated protein, and

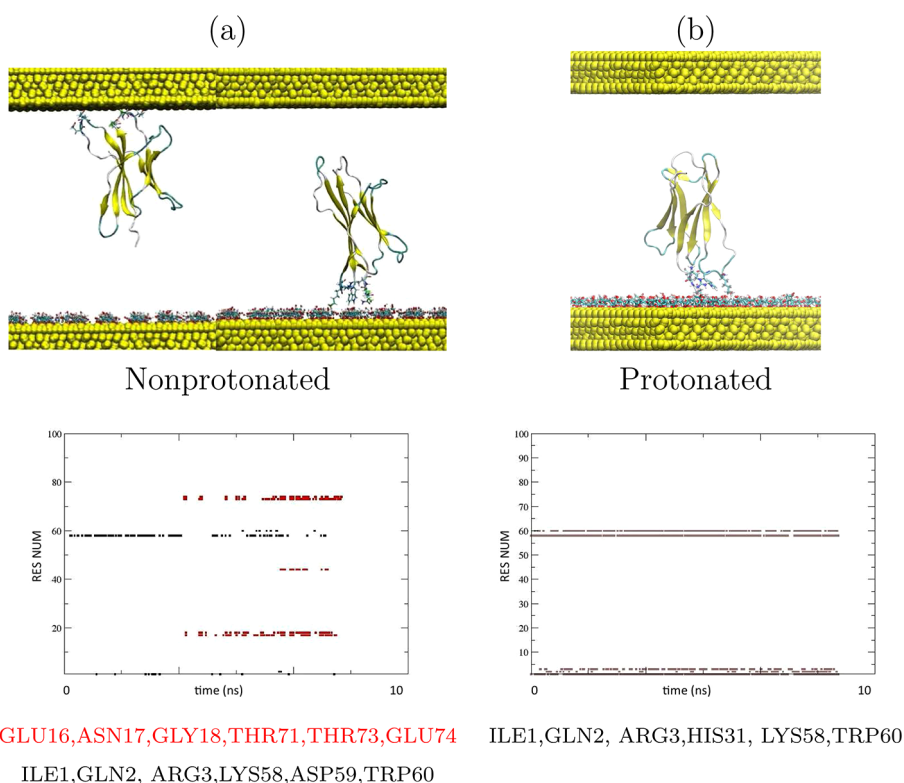


Figure 4. (a) Nonprotonated protein and (b) protonated protein. Top panel (a) shows the most representative structures of the nonprotonated protein during T-REMD, and top panel (b) shows the orientation for the protonated protein on cit-AuNPs. In both cases, the results are obtained following the replica at the lowest temperature during 20 ns of T-REMD. Bottom panels (a,b) report the time evolution of contacting residues (*i.e.*, residues with atoms within 0.6 nm from the Au surface) for the nonprotonated and protonated protein with respect to the surface of the nanoparticle, extracted from the last 10 ns of the total 20 ns T-REMD.

325 Figure 4b shows the unique stable orientation for the
 326 protonated protein. In both cases, the results were
 327 obtained following the replica at the lowest tempera-
 328 ture during the 20 ns of T-REMD. The bottom panels of
 329 Figure 4a,b report the time evolution of contacting
 330 residues for the nonprotonated (a) and protonated (b)
 331 protein with respect to the surface of the nanoparticle,
 332 along the last 10 ns of T-REMD. In the case of the
 333 nonprotonated protein, the patch contacting the citra-
 334 te surface is not conserved during the simulation,
 335 which points to a loosely bound neutral protein on the
 336 top of cit-AuNPs. On the contrary, for the protonated
 337 protein (Figure 4b), the contact patch is unique and
 338 well conserved during the entire 20 ns length of T-REMD
 339 since the protein is never able to detach from the citrate
 340 layer during the 20 ns but it remains anchored through
 341 the N-terminal residues (ILE1, GLN2, ARG3) and DE loop
 342 residues (LYS58, TRP60). The capability of the nonpro-
 343 tonated protein to detach from the citrate surface
 344 during T-REMD is in line with the labile, transient
 345 interaction measured by the experiments (as will be
 346 discussed in the next sections).

347 The structural impact on (i) nonprotonated and (ii)
 348 protonated proteins upon adsorption on the top of the
 349 cit-Au(111) surface was analyzed with an additional
 350 conformational analysis (sorting and averaging of the

trajectories) of the simulated systems to select a few
 representative structures of the proteins contacting
 the cit-Au(111) through the N-terminal tail. Clustering
 with a simple means algorithm was applied during the
 last 5 ns of the 20 ns T-REMD, extracting (i) one relevant
 representative structure for the nonprotonated protein
 and (ii) six relevant representative structures for the
 protonated protein (shown in Figure 5) covering the
 50% of the total population in both cases.

The unique nonprotonated structure has a root-
 mean-square deviation (rmsd) value of 1.96 Å with
 respect to the NMR reference structure (PDB code
 1JNJ), pointing to modest internal rearrangements of
 the nonprotonated protein. On the contrary, protonated
 structures have rmsd with respect to NMR refer-
 ence (PDB code 1JNJ modified by protonation of HIS31
 residue) ranging from 2.15 to 3.45 Å, referring to local
 rearrangements of loops AB, DE, BC, and strand D (see
 Figure 5). In all cases, the internal rearrangements of
 the proteins suggest the absence of unfolding events
 in the short term that are able to destructure the
 secondary structure of the native protein. However,
 the larger rmsd and the larger variety of structures
 observed for the protonated protein point to a lower
 stability of the system under acidic conditions upon
 adsorption on cit-Au. Moreover, a deeper analysis

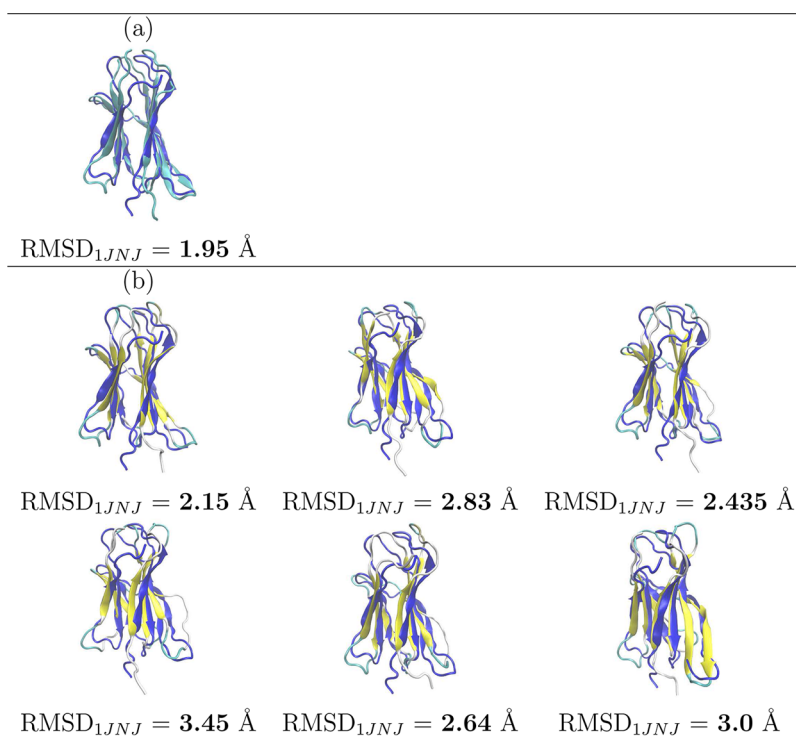


Figure 5. Cluster analysis of the conformational rearrangements of the protein on cit-AuNPs during the last 5 ns of the 20 ns of T-REMD following replica at the lowest temperature and computed rmsd with respect to the NMR reference structure. (a) Nonprotonated protein and (b) protonated protein. Resulting structures cover 50% of the total population in both cases.

377 showed that, among the structures with the largest
 378 rmsd with respect to the NMR reference, the largest
 379 deviations were localized at the BC loop region, which
 380 belongs to the hydrophobic pocket formed by the
 381 N-terminus, BC and FG loop, as discussed in ref 47. To
 382 quantify, the rmsd values restricted to the atoms of the
 383 BC loop (residues 31–34) were evaluated and found to
 384 range from (i) 2.5 Å for the nonprotonated case to (ii)
 385 3.4 Å for the protonated case, with respect to the NMR
 386 reference. For the sake of comparison, the same rmsd
 387 values restricted to the BC loop (for the nonprotonated
 388 β_2m) were compared with that of the same protein
 389 interacting with a hydrophobic nanoparticle ($Au_{25}L_{18}^-$,
 390 $L = S(CH_2)_2Ph$) through the same hydrophobic patch.⁵⁵
 391 In that case, the rmsd value was only 1.6 Å. The
 392 reported behavior points to an induced larger expo-
 393 sure of the protonated HIS31 side chains upon adsorp-
 394 tion to hydrophilic surfaces with respect to hydro-
 395 phobic surfaces. The native *cis*-prolyl peptide bond
 396 (between HIS31 and PRO32) switches to *trans* as part
 397 of the transition to the amyloidogenic state. It is well-
 398 known that the conversion of the HIS31–PRO32 pep-
 399 tide bond from *cis* to *trans* requires the breaking of a
 400 network of hydrogen bonds⁵⁶ and of the interactions
 401 stabilizing the hydrophobic pocket.⁴⁷ This transition
 402 may therefore be catalyzed by the interactions of
 403 N-terminal residues with the adlayer of citrate. We
 404 were not able to observe the *cis*–*trans* transition in
 405 our simulations, due to the low probability of the event
 406 and the length of the simulations. To understand if the

citrate adlayer has a role in the conformational rear-
 rangements of the protonated protein, we have
 repeated the same 20 ns T-REMD simulation for the
 protein in bulk solution (same number of replicas).
 Focusing on the BC loop, we observed a decrease in the
 rmsd from 3.4 Å on cit-AuNP to 2.2 Å in solution for the
 protonated case (the rmsd of the entire protein also
 decreased). These findings indicate that the citrate
 adlayer magnifies the conformational changes related
 to protein protonation. To investigate this point
 further, we additionally performed configurational
 principal component analysis to reveal the structures
 underlying the atomic fluctuations and the region of
 the protein with the highest degree of correlation,
 which may be directly connected through bonds or
 move in a concerted manner. In Figure 6, we report a
 direct comparison between the first three dominant
 fluctuations of the (i) nonprotonated and (ii) proton-
 ated protein in solvent and upon interaction with the
 cit-AuNPs. In the case of (i) nonprotonated protein, the
 largest collective motions of atoms are localized at the
 N-terminal tail and DE loop regions, whereas in the (ii)
 protonated case, fluctuations of the BC loop, involving
 the HIS31–PRO32 peptide bond, are more relevant
 especially in the vicinity of the adlayer of citrate (see
 modes 1 and 2 in Figure 6) and appear to be slightly
 correlated to the fluctuation of the proximal DE loop
 belonging to the same hydrophobic pocket. More in
 detail, fluctuations at the BC loop appear to be larger
 when fluctuations at the DE loop are larger. On the

407
 408
 409
 410
 411
 412
 413
 414
 415
 416
 417
 418
 419
 420
 421
 422
 423
 424
 425
 426
 427
 428
 429
 430
 431
 432
 433
 434
 435
 436

F6

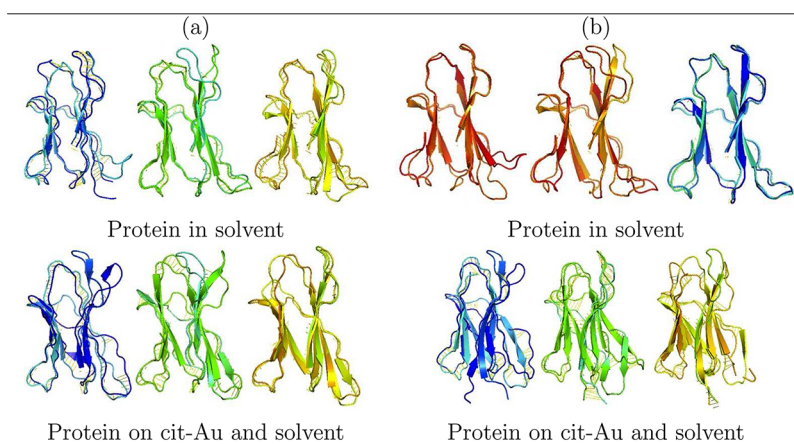


Figure 6. Principal component analysis: direct comparison between the first three dominant fluctuations of the (a) nonprotonated protein and (b) protonated protein in solvent and upon interaction with the cit-AuNPs. Protonated and nonprotonated proteins in solvent exhibit very similar dynamics, while the protonated protein on the surface has distortions notably larger than that of the nonprotonated one.

437 contrary, fluctuations at the BC and DE loop appear to
 438 be larger when fluctuations at the AB loop are smaller
 439 and *vice versa*. The comparison clearly shows the role
 440 of the interaction with the charged surface of cit-
 441 AuNPs on the induced conformational changes of
 442 the protonated protein, which are absent in water
 443 and much more limited for the nonprotonated case.

444 To summarize, with a number of T-REMD refining
 445 runs, we were able to assess the global stability of
 446 complex A already predicted by rigid-body BD docking
 447 on the top of negatively charged AuNPs. The protein
 448 was always contacting the nanoparticle through the
 449 apical region representing the edges of the D and E
 450 β -strand and N-terminal tail. The protonated and non-
 451 protonated forms of the proteins showed quite differ-
 452 ent stability when interacting with the citrate layer
 453 (largest changes and fluctuations for the protonated).
 454 In particular, the comparison between the protonated
 455 β_2 m behavior in solution and interacting with the
 456 citrates suggests that the latter accentuate the struc-
 457 tural destabilization following protonation.

458 **Role of Nanoparticle Actual Size on the Electrostatic Inter-**
 459 **action.** In order to support the assumption based on a flat
 460 surface, the nanoparticle coated by citrate was addi-
 461 tionally simulated by a dielectric sphere with a diam-
 462 eter of 5 nm (as in the experiments) and with the
 463 same density of negative charge as in the Brownian
 464 dynamics model ($-1.38 e/nm^2$).

465 Because the goal of this model was to test the effect
 466 of finite particle size on electrostatic characteristics,
 467 only electrostatic interactions were considered. It was
 468 also assumed, based on explicit computations for a few
 469 randomly selected rotamers, that the generalized Born
 470 radii of the atoms are not changed significantly by the
 471 presence of the nanoparticle, as long as the two
 472 systems remain well separated.

473 Generalized Born radii have been computed ac-
 474 cording to the GBR6 model, which was shown to be

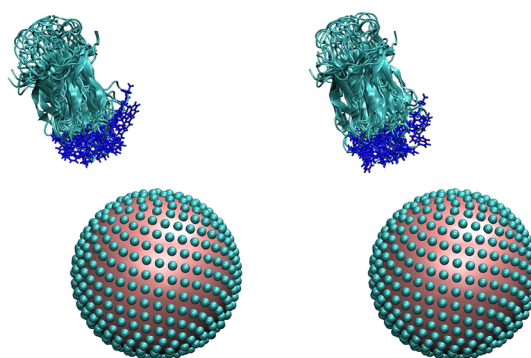


Figure 7. Ten lowest energy arrangements of β_2 -microglobulin (shown together) and a model of a citrate-coated nanoparticle for the neutral protein (left panel) and positively charged protein (right panel). Citrate moieties are modeled as 3 Å spheres on the surface of a 25 Å sphere representing the nanoparticle. The side chains of residues 1, 3, 31, 59, and 60 of the protein are shown in blue.

475 extremely accurate for proteins.⁵⁷ The set of 10 rota-
 476 mers leading to the system's lowest electrostatic
 477 energy are superimposed and displayed in Figure 7
 478 for the neutral and positively charged states of β_2 -
 479 microglobulin.

480 The number of favorable orientations and the
 481 computed interaction energies depend on the dis-
 482 tance between the centers of mass, on the radius
 483 assumed for the citrate particles, and on the charge
 484 state of the protein. For the neutral state, there are 384
 485 favorably interacting orientations out of 800, whereas
 486 for the positively charged state, the same figure rises to
 487 425. Notwithstanding these differences, it is seen that
 488 for all orientations the N-terminal region is pointing
 489 toward the negative nanoparticle. The same conclu-
 490 sion holds for all of the possible 16 protonation
 491 states of the four histidines, although the number of
 492 favorably interacting orientations and the interaction
 493 energy depends on the histidines' protonation state
 494 (data not shown).

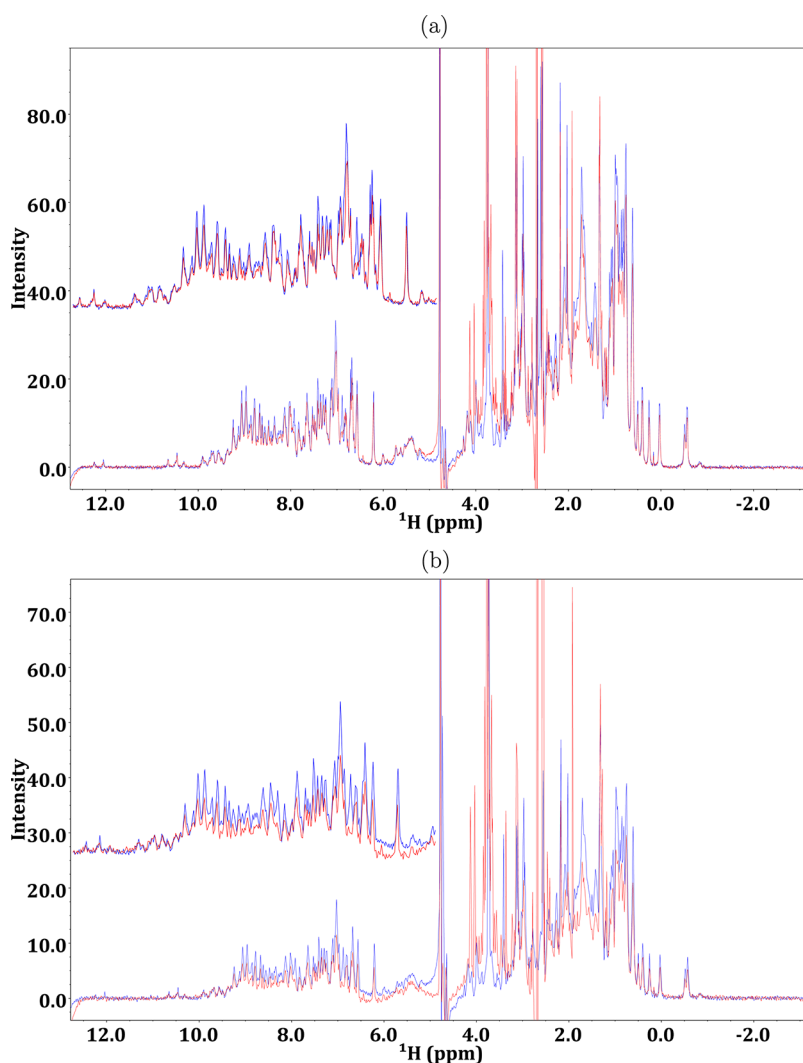


Figure 8. One-dimensional ^1H NMR spectra: In blue and red are the traces of the protein alone and in the presence of gold nanoparticles at 130 nM, pH 6.47, and 298 K. The protein concentration is 36 and 17 μM in (a) and (b), respectively. A few limited changes are seen upon adding Au nanoparticles. Among these, we can identify shifts of the phenyl hydrogens of F56 around 6.5 and 6.9 ppm (the corresponding amide resonances, however, do not undergo any shift; see the HSQC map in Supporting Information). In addition, we see the intensity loss of the N42 side chain amide around 8 ppm and the slight chemical shift changes of S28 and L40 backbone amides at about 9 ppm. On the other hand, the differences that are seen in the aliphatic region are due to citrate and stabilizing surfactants that occur in the nanoparticle preparations.

495 **NMR Experimental Evidence.** One-dimensional ^1H and
 496 2D [^1H , ^{15}N] HSQC NMR experiments have been used
 497 to characterize, at amino acid residue level, the inter-
 498 action between $\beta_2\text{m}$ and gold nanoparticles at
 499 various molar ratios. Different samples containing
 500 130 nM of 5 nm AuNP (Sigma-Aldrich) and variable
 501 $\beta_2\text{m}$ concentrations ranging from 4 to 36 μM were
 502 analyzed.

503 A general decrease of $\beta_2\text{m}$ signal intensity in ^1H
 504 monodimensional experiments when Au nanoparti-
 505 cles were added is highlighted in Figure 8, whereas
 506 chemical shifts are only marginally affected.

507 In fact, the presence of nanoparticles affects the
 508 protein signal intensities much more than chemical
 509 shifts. The attenuation tends to decrease as the protein
 510 concentration increases and arises from exchange
 511 average between the free molecule and the species

transiently in contact with the nanoparticle. Due to the
 slower tumbling of the protein nanoparticle adduct
 with respect to the free molecule, the resulting larger
 extent of dipolar broadening propagates to the free
 species because of fast exchange, thereby attenuating
 the overall sampled signal. This behavior is consistent
 with protein–nanoparticle interactions also confirmed
 by a surface plasmon resonance absorption red shift of
 3.4 nm shown in Figure 9.

512
 513
 514
 515
 516
 517
 518
 519
 520 **F9**
 521 Similar shifts were reported for hUbcq and azurin.²⁶
 522 The comparison of 1D spectra of $\beta_2\text{m}$ alone and with
 523 AuNP presence suggests the absence of any significant
 524 chemical shift perturbation that is confirmed by the
 525 complete cross-peak overlap of HN signals in 2D
 526 [^1H , ^{15}N] HSQC maps acquired with and without nano-
 527 particles (results are shown in Figure 2 of Supporting
 528 Information).

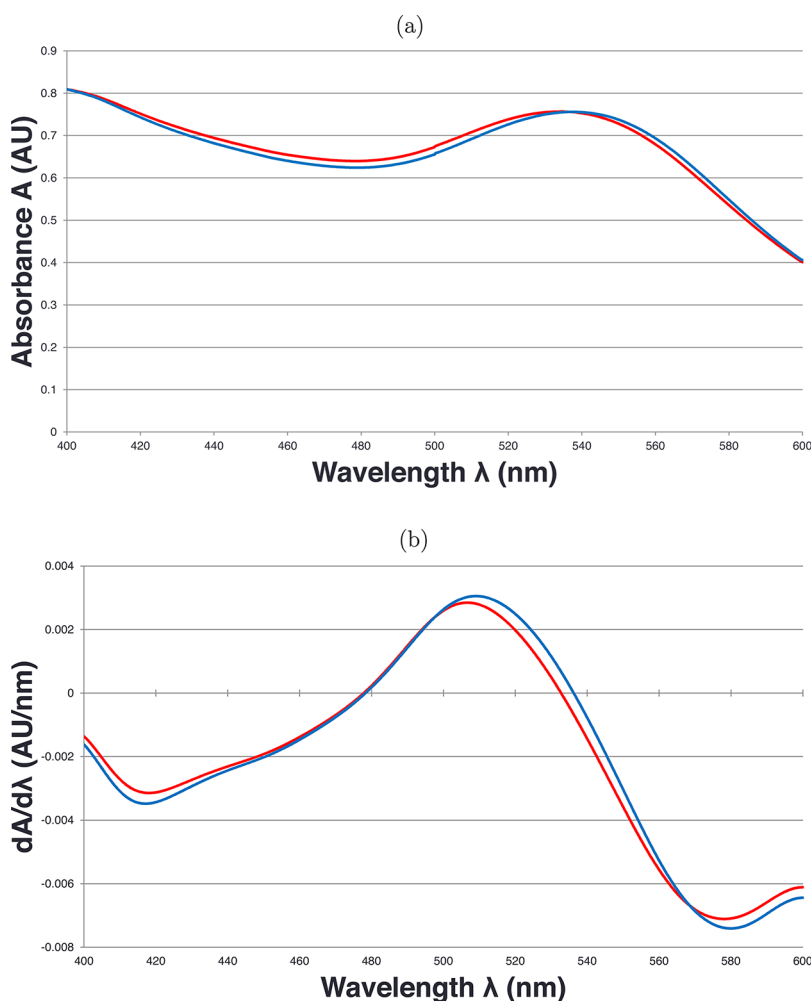


Figure 9. UV–vis spectra of AuNP free and bound to β_2m in red and blue, respectively. AuNP and β_2m are at a concentration of 130 nM and 26 μM . (a) UV–vis spectrum and (b) spectrum derivative highlight the surface plasmon resonance red shift of 3.4 nm.

529 This is the signature of a conserved protein fold also
 530 when the protein interacts with the gold–citrate surface.
 531 On the contrary, the analysis of the normalized
 532 cross-peak intensities, shown in Figure 10, reveals
 533 differential behaviors of the observed HN connectivity
 534 signals, suggesting variable dipolar contributions
 535 to relaxation for the various amide locations that
 536 approach the surface of the AuNPs more closely.

537 Simple steric consideration, based on the protein
 538 modeled as a sphere or with an oblate shape, has led to
 539 speculation that 15–25 molecules can be accommodated
 540 in a layer surrounding a 5 nm diameter nanoparticle.
 541 These estimates are probably in excess because a very
 542 close packing is implied but tell us that in the present
 543 experimental conditions, even at the lowest tested
 544 β_2m concentration, the number of protein molecules
 545 largely exceeds the amount required to cover the
 546 particle surface. Therefore, the present results reflect
 547 the fast exchange between the bound and free state
 548 of the protein, in the context of a labile protein–
 549 nanoparticle adduct. This, in turn, suggests a weakly
 550 bound protein layer surrounding the NPs, also

referred to as soft corona;¹³ even if the corresponding
 hard corona would be poorly observable by NMR
 because of an expected rather slow rotational tumbling
 rate, there are a few elements that make the occurrence
 of a tightly bound layer of β_2m around the small
 AuNPs unlikely. First, the size of the NPs is not
 that large to support a tightly bound first corona
 layer.¹³ The actual interaction between the citrate-
 coated surface of the NPs and the protein should be
 electrostatic, as confirmed by simulation, but the
 overall protein charge should be around zero or
 slightly negative, which definitely attenuates the
 layer tightness. The substantial agreement between
 simulation and experiment for the NP close approach
 or contact points on the protein surface suggests that
 the loosely bound layer of protein molecules we
 observe experimentally does not establish contacts
 with any hard corona layer of protein molecules.
 The experimental differential attenuation pattern,
 on the other hand, cannot be attributed to the
 citrate because control experiments (not shown)
 confirm the absence of any correlation between
 the pattern observed with citrate-coated

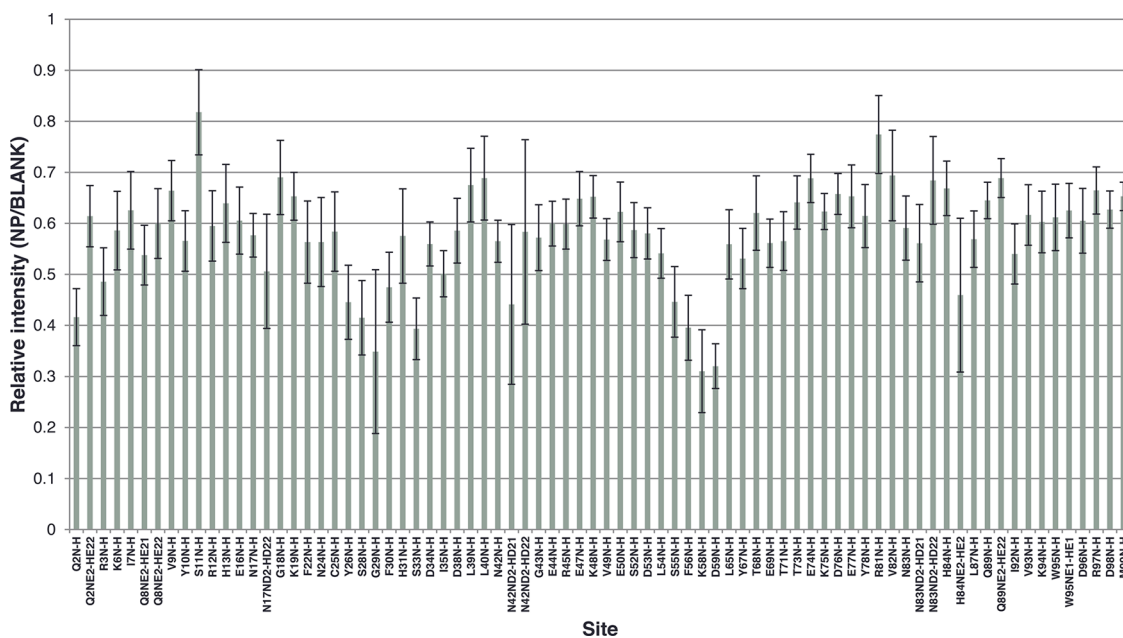


Figure 10. Relative intensities of $\beta_2\text{m}$ HSQC cross-peaks in the free and bound state at a protein concentration of $17\ \mu\text{M}$.

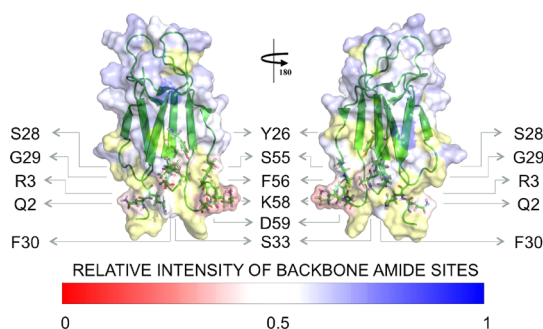


Figure 11. β_2 -Microglobulin surface colored according to the relative intensity scale. The residues whose backbone amide sites have less than 0.5 relative intensities are highlighted. Amide residues not measured in the analysis are in yellow.

573 AuNPs and that obtained with citrate alone. The
574 described weak interaction regime appears to be consis-
575 tent with the experimentally observed attenuation
576 pattern of the protein signals. The normalized inten-
577 sities in Figure 10 for the backbone amide peaks
578 obtained from the $26\ \mu\text{M}$ sample are highlighted on
579 the $\beta_2\text{m}$ molecular structure in Figure 11 (PDB code
580 1JNJ) through appropriate color coding.

581 The picture renders the involvement in the interac-
582 tion with AuNPs of the N-terminal apical part of the
583 protein, in particular, GLN2 and ARG3 in the N-terminus
584 and LYS58 and ASP59 in the DE loop, in good agree-
585 ment to complex A of the simulations, as already
586 discussed in Figure 3. In addition, we could also identify
587 other close interaction sites, in the DE loop, SER55 and
588 PHE56 in strand B, and residues TYR26, SER28, GLY29,
589 PHE30, and SER33 in the following BC loop. This
590 interaction pattern is proven to be independent from
591 the experimental protein/nanoparticle molar ratio.
592 Very similar pictures emerged, in fact, when the $\beta_2\text{m}$

concentration was lowered to $4\ \mu\text{M}$ with a $\beta_2\text{m}/\text{AuNP}$
ratio of about 30. The same residue involvement was
assessed with the addition of LYS6, ASN42, and LEU65.
These additional involvements may reflect the less-
populated binding modes which are expected to occur
from rigid docking (see Supporting Information) and
whose occurrence should be more easily observed at
low protein concentration excess with respect to
AuNPs. To test a long-term effect of AuNP on $\beta_2\text{m}$
stability, we repeatedly acquired HSQC spectra over
4–7 days from sample preparation—and more recently
over about a month with an analogous system—
without revealing any significant variation (data not
shown). This result establishes over macroscopically
accessible time frames the conformational stability
elements observed in T-REMD analysis.

CONCLUSIONS

In this article, we have presented an extensive set of
experimental and computational studies of the interac-
tion between $\beta_2\text{m}$ and citrate-capped gold NPs. We
have used atomically detailed simulations at multiple
levels of theory, including docking by Brownian
dynamics, Poisson–Boltzmann electrostatics, and
enhanced atomistic MD. From these simulations, we
could provide molecular insights into the $\beta_2\text{m}$ –
cit–AuNP interactions that are not directly accessible
from experiments. In particular, on the basis of our
results on protein–surface docking and implicit solva-
tion modeling, we discussed the nature of the interac-
tions that guide the binding of $\beta_2\text{m}$ to the citrate-
capped gold nanoparticle, finding that long-range
electrostatic interactions are the leading terms for
the encounter complex. In fact, the orientation of the
protein relative to the particle surface is determined by

627 such interactions and is in agreement with the experi-
 628 mental results from NMR spectroscopy. Moreover, the
 629 comparison between docking results obtained by
 630 mimicking the experimental conditions clearly shows
 631 that the adlayer of citrate molecules does remain on
 632 the surface of the NP, coexisting with the adsorbed
 633 protein, similarly to what was previously shown for
 634 other proteins on cit-AuNPs.^{27,58} Both experiments
 635 and simulations suggest that the internal rearrange-
 636 ments of the protein induced by the interaction with
 637 the charged surface of cit-AuNPs are not able to
 638 disrupt the secondary structure of the native protein
 639 thus do not lead to unfolded amyloidogenic inter-
 640 mediates. The overall picture is consistent with the
 641 small dimensions of the AuNPs and the labile inter-
 642 action regime that occurs between β_2m and the
 643 AuNPs. Our MD results also suggest that the effects

of protonation of HIS31, known to destabilize the
 protein toward amyloidogenic intermediates, are en-
 hanced by the interaction with the negative surface.
 Our work also offers a fresh view on the interaction of
 the protein with biomolecules comprising negative
 charge arrays.

The results presented here, combined with our
 previous findings on hydrophobic NPs,⁵⁵ suggest that,
 by properly balancing the extent of electrostatic and
 hydrophobic interactions, the NP surface may provide
 stabilization/destabilization to amyloidogenic proteins
 as shown in the comparison between nonprotonating
 and protonating conditions. Therefore, NP-based ap-
 proaches to treat amyloid pathologies may be defi-
 nitely conceived once the available ingredients for NP
 performance are adapted to the properties of the
 specific protein surface.

662 METHODOLOGY

663 **Electrostatic Model.** The structure of β_2 -microglobulin (PDB
 664 code 1JNJ) was preprocessed using PDB code 2PQR⁵⁹ using the
 665 CHARMM set of radii and charges. In view of the high negative
 666 potential due to the nanoparticle, HIS51 for which a pK_a of 6.6 is
 667 predicted using the program BLUUES⁵⁷ was assigned a protonated
 668 state. The overall charge of the protein is important for
 669 the absolute value of the interaction with the nanoparticle, but
 670 the best orientations are less sensitive to it. In the presence of a
 671 negatively charged nanoparticle (and consequent local pH
 672 lowering), it is expected that the overall charge state of the
 673 protein should be close to zero at measured pH 6.5. The
 674 structure of β_2 -microglobulin was placed 65 Å distance from
 675 the center of the nanoparticle rotated around 100 axes uni-
 676 formly distributed in the solid angle and identified by the polar
 677 angular coordinates θ and ϕ . The rotation angle ψ about the axis
 678 was taken from a distribution with probability density

$$\frac{2}{\pi} \sin^2\left(\frac{\psi}{2}\right) = \frac{1}{\pi} (1 - \cos(\psi)) \quad (1)$$

679 for uniformly sampling the rotation space. The total number of
 680 rotations sampled was 800.

681 **NMR Spectroscopy.** The interaction between β_2m and AuNP
 682 was studied by NMR experiments and UV–vis absorption
 683 spectroscopy on samples containing Au nanoparticles at a
 684 concentration of 130 nM. NMR experiments were performed
 685 at β_2m concentrations of 4, 17, 26, and 36 μM . All samples
 686 analyzed were buffered with 25 mM sodium phosphate, pH 6.4,
 687 and contained 5% D₂O for lock purposes. NMR experiments
 688 were recorded on a Bruker Avance spectrometer operating at
 689 500 MHz (¹H). The 1D ¹H spectra were acquired with 4096 data
 690 point, a spectral width of 16 ppm, and 4096 scans. The water
 691 suppression was achieved by an excitation sculpting scheme.⁶⁰
 692 The 2D and [¹H, ¹⁵N] HSQC spectra were acquired with 1024 and
 693 128 points in the direct and indirect dimensions, respectively,
 694 and 400–1600 scans depending on the sample concentration,
 695 over spectral widths of 16 and 37 ppm in the ¹H and ¹⁵N
 696 dimensions, respectively. The data were processed with Top-
 697 spin 2.1 and analyzed with NMRViewJ.⁶¹ The β_2m assignment
 698 was based on the file deposited on the Biological Magnetic
 699 Resonance Data Bank (accession code 17165). AuNPs, 5 nm in
 700 diameter, 0.01% in HAuCl₄ (around 130 nM in NP concentra-
 701 tion), were purchased by Sigma-Aldrich (product code G1402)
 702 and used without further purification after UV–vis test to verify
 703 that no aggregation has taken place.

704 **UV–Vis Absorption Spectroscopy.** A spectrum in the range from 400
 705 to 600 nm was acquired with a JASCO UV-530 spectrophotometer

on samples containing Au nanoparticles and β_2m at a concentra-
 tion of 130 nM and 26 μM , respectively. The experimental condi-
 tions for the solutions were the same as those for NMR samples;
 1001 points were acquired with a bandwidth of 2.0 nm, a data pitch
 of 0.2 nm, and a speed of 40 nm/min.

711 **Brownian Dynamics Simulations.** Rigid-body docking simu-
 712 lations were carried out using Brownian dynamics techniques
 713 with the ProMetCS continuum solvent model for protein–gold
 714 surface interactions.⁴⁰ The calculations were performed using
 715 the SDA version 6 software.^{62,63} The Au(111) surface was con-
 716 structed with a surface area of 100 Å × 100 Å and three atomic
 717 layers.⁶⁴ The β_2m structure was taken from the NMR solution
 718 structure (PDB code 1JNJ). Human β_2m is a 99 residue long,
 719 11.9 kDa protein, with a single disulfide bridge between the two
 720 CYS residues of the sequence at positions 25 and 80. The protein
 721 folds into the classical β -sandwich motif of the immunoglobulin
 722 superfamily, that is, seven antiparallel β -strands (A, B, ..., G),
 723 forming two facing sheets (ABED and CFG).⁶⁵

724 Five thousand BD trajectories were computed starting with the
 725 protein positioned randomly with its center at a distance of
 726 70 Å from the surface where the protein–surface interaction
 727 energy is negligible. The specified number of docked com-
 728 plexes was extracted directly from the runs and clustered with a
 729 clustering algorithm. Experimental salt concentration of 30 mM
 730 was included as a nonspecific screening effect on the electro-
 731 static potential of the protein, which was calculated using the
 732 APBS program.⁶⁶ The relative translational diffusion coefficient
 733 was 0.0123 Å²/ps, and the rotational diffusion coefficient for the
 734 protein was 1.36 × 10^{−4} radian²/ps. The simulation time step
 735 was set to 0.50 ps. Parameters for the calculation of hydro-
 736 phobic desolvation energy and forces were set to −0.019 kcal/
 737 mol/Å² and for the electrostatic desolvation energy and forces
 738 to 1.67 according to ref 67. BD trajectories were generated in a
 739 rectangular box (ibox = 1); the dimensions of the (x,y) plane,
 740 describing the symmetry of the simulation volume as well as the
 741 surface size, were given as input parameters. At each BD step,
 742 the protein–surface interaction energy and forces acting on the
 743 protein were computed using the implicit solvent ProMetCS
 744 force field,⁴⁰ developed and parametrized for protein–gold
 745 surface interactions. The energy terms included in ProMetCS
 746 have been described in the main text.

747 Two clustering algorithms were tested and evaluated for this
 748 system. These were top-down splitting (hierarchical based on a
 749 reference structure) and bottom-up aggregating (single-linkage
 750 based on rmsd). The results of docking were preprocessed by
 751 translating the protein coordinates parallel to the surface in
 752 order to superimpose the protein structures before applying the
 753 clustering algorithm. Finally, we applied a single-linkage

754 clustering method (based on CA atoms, with rmsd = 3.0 Å) for
755 the results given in the article.

756 **Molecular Dynamics Simulations.** We have implemented new
757 force field parameters for the citrate anions based on *ab initio*
758 calculations (that take into account the quantum nature of such
759 small chemical species) in a consistent and compatible way with
760 the existing GoIP force field for the protein–AuNP surface
761 interactions.

762 The regular citrate adlayer on the top of Au(111) was
763 generated with a ratio of the surface gold ion and citrate
764 concentrations suitable to reproduce experimental data.³⁹ The
765 positive atomic charges of the gold surface atoms were set to fit
766 the electronic charges/cm² on the surface of the AuNPs in the
767 electrochemical experiments under aqueous conditions and at
768 physiological pH.³³

769 For the (i) nonprotonated β_2m , all titratable protein side
770 chains were assigned their standard protonation state at pH 6.8
771 using the H++ pK calculation program;⁶⁸ (ii) for the protonated
772 protein, additional protonation at HIS31 was performed.

773 At the beginning of the simulation, the protein was moved
774 away from the surface of the cit-AuNPs by 6 Å, without changing
775 the orientation that resulted from docking. Various tests that we
776 performed showed that the protein in direct contact with the
777 surface is in a kinetically trapped state were only minor relaxa-
778 tion can take place on the time scale of tens of nanoseconds.

779 For each (i) nonprotonated and (ii) protonated protein,
780 32 replicas of a rectangular simulation box with dimension of
781 82 Å × 64 Å × 82 Å, including SPC water molecules, the protein,
782 the citrate adlayer, and the gold surface were built.

783 Before the solvent was added in the box, the protein was
784 moved away from the surface of the cit-AuNPs by 6 Å, without
785 changing the orientation that resulted from docking. Various
786 tests that we performed showed that the protein in direct
787 contact with the surface is in a kinetically trapped state, where
788 only minor relaxation can take place on the time scale of tens
789 of nanoseconds. All simulations were performed with the
790 Gromacs 4.5.4 package.⁶⁹ GoIP⁶⁴ and OPLS/AA parameters⁷⁰
791 were used for the surface and the protein, and the SPC/E water
792 model⁷¹ was applied. The bond lengths were constrained with
793 the LINCS algorithm. Surface gold atoms and bulk gold atoms
794 were frozen during all simulations, but gold dipole charges
795 were left free. Periodic boundary conditions and the particle
796 mesh Ewald algorithm were used. A 2 fs integration time step
797 was used.

798 We performed a total of four independent T-REMD simula-
799 tions of 20 ns in explicit water for both (i) nonprotonated and (ii)
800 protonated protein in solvent and on the top of the cit-Au(111)
801 surface in the temperature range of 290–320 K.

802 Trajectories were analyzed in terms of density, temperature,
803 potential energy, and other macroscopic properties with the
804 Gromacs tools (e.g., g_traj, g_rms, g_clusters, etc.). Principal
805 component analysis was also performed using GROMACS, and
806 to compare principal component obtained from independent
807 runs, the covariance matrix was calculated. The eigenvectors
808 and eigenvalues were obtained from diagonalization of the
809 combined covariance matrix, after which coordinates from each
810 independent trajectory were projected along eigenvectors of
811 interest to obtain projection values for given modes.

812 **Conflict of Interest:** The authors declare no competing
813 financial interest.

814 **Acknowledgment.** Funding from MIUR through PRIN
815 2012A7LMS3_003 is gratefully acknowledged. This work was
816 funded by the Italian Institute of Technology through Platform
817 Computations and Seed project “MOPROSURF—MOdeling
818 PROtein SURface interactions”. The IS CRA staff at CINECA
819 (Bologna, Italy) are acknowledged for computational facilities
820 and technical support. Oak Ridge National Laboratory by the
821 Scientific User Facilities Division, Office of Basic Energy Sciences,
822 U.S. Department of Energy is acknowledged for the super-
823 computing project CNMS2013-064. Facilities of the National
824 Energy Research Scientific Computing Center (NERSC), which is
825 supported by the Office of Science of the U.S. Department of
826 Energy under Contract No. DE-AC02-05CH11231, are also
827 acknowledged.

Supporting Information Available: Additional figures and 828
table. This material is available free of charge via the Internet 829
at <http://pubs.acs.org>. 830

REFERENCES AND NOTES

1. Lundqvist, M.; Stigler, J.; Elia, G.; Lynch, I.; Cedervall, T.; Dawson, K. A. Nanoparticle Size and Surface Properties Determine the Protein Corona with Possible Implications for Biological Impacts. *Proc. Natl. Acad. Sci. U.S.A.* **2008**, *105*, 14265–14270. 831
2. Maiorano, G.; Sabella, S.; Sorce, B.; Brunetti, V.; Malvindi, M. A.; Cingolani, R.; Pompa, P. P. Effects of Cell Culture Media on the Dynamic Formation of Protein–Nanoparticle Complexes and Influence on the Cellular Response. *ACS Nano* **2010**, *4*, 7481–7491. 832
3. Lacerda, S. H. D. P.; Park, J. J.; Meuse, C.; Pristinski, D.; Becker, M. L.; Karim, A.; Douglas, J. F. Interaction of Gold Nanoparticles with Common Human Blood Proteins. *ACS Nano* **2010**, *4*, 365–379. 833
4. Mahmoudi, M.; Lynch, I.; Ejtehadi, M. R.; Monopoli, M. P.; Bombelli, F. B.; Laurent, S. Protein–Nanoparticle Interactions: Opportunities and Challenges. *Chem. Rev.* **2011**, *111*, 5610–5637. 834
5. Moyano, D. F.; Rotello, V. M. Nano Meets Biology: Structure and Function at the Nanoparticle Interface. *Langmuir* **2011**, *27*, 10376–10385. 835
6. Pelaz, B.; Jaber, S.; de Aberasturi, D. J.; Wulf, V.; Aida, T.; de la Fuente, J. M.; Feldmann, J.; Gaub, H. E.; Josephson, L.; Kagan, C. R.; et al. The State of Nanoparticle-Based Nanoscience and Biotechnology: Progress, Promises, and Challenges. *ACS Nano* **2012**, *6*, 8468–8483. 836
7. Gobin, A.; Lee, M.; Halas, N.; James, W.; Drezek, R.; West, J. L. Near-Infrared Resonant Nanoshells for Combined Optical Imaging and Photothermal Cancer Therapy. *Nano Lett.* **2007**, *7*, 1929–1934. 837
8. Lu, F.; Doane, T. L.; Zhu, J.-J.; Burda, C. Gold Nanoparticles for Diagnostic Sensing and Therapy. *Inorg. Chim. Acta* **2012**, *3006*, 1–12. 838
9. Wright, J. Deliver on a Promise. *Nature* **2013**, *509*, S58–S59. 839
10. Gibbs, B. F.; Yasinska, I. M.; Calzolari, L.; Gilliland, D.; Sumbayev, V. V. Highly Specific Targeting of Human Leukocytes Using Gold Nanoparticle-Based Biologically Active Conjugates. *J. Biomed. Nanotechnol.* **2014**, *10*, 1259–1266. 840
11. Nel, A. E.; Mädler, L.; Velegol, D.; Xia, T.; Hoek, E. M. V.; Somasundaran, P.; Klaessig, F.; Castranova, V.; Thompson, M. Understanding Biophysicochemical Interactions at the Nano-Bio Interface. *Nat. Mater.* **2009**, *8*, 543–557. 841
12. Dawson, K. A.; Salvati, A.; Lynch, I. Nanotoxicology: Nanoparticles Reconstruct Lipids. *Nat. Nanotechnol.* **2009**, *4*, 84–85. 842
13. Rahaman, M.; Laurent, S.; Tawil, N.; Yahia, L.; Mahmoudi, M. *Protein–Nanoparticle Interactions*; Springer-Verlag: Berlin, 2013; Chapter 2, pp 21–44. 843
14. Saptarshi, S. R.; Duschl, A.; Lopara, A. L. Interaction of Nanoparticles with Proteins: Relation to Bio-reactivity of the Nanoparticle. *J. Nanobiotechnol.* **2013**, *11*, 26–37. 844
15. Cabaleiro-Lago, C.; Quinlan-Pluck, F.; Lynch, I.; Dawson, K. A.; Linse, S. Dual Effect of Amino Modified Polystyrene Nanoparticles on Amyloid β Protein Fibrillation. *ACS Chem. Neurosci.* **2010**, *1*, 279–287. 845
16. Lynch, I.; Dawson, K. A. Protein–Nanoparticle Interactions. *Nano Today* **2008**, *3*, 40–47. 846
17. Liao, Y.-H.; Chang, Y.-J.; Yoshiike, Y.; Chang, Y.-C.; Chen, Y.-R. Negatively Charged Gold Nanoparticles Inhibit Alzheimer’s Amyloid- β Fibrillization, Induce Fibril Dissociation, and Mitigate Neurotoxicity. *Small* **2012**, *8*, 3631–3639. 847
18. Zhang, M.; Mao, X.; Yu, Y.; Wang, C.-X.; Yang, Y.-L.; Wang, C. Nanomaterials for Reducing Amyloid Cytotoxicity. *Adv. Mater.* **2013**, *25*, 3780–3801. 848
19. Mahmoudi, M.; Kalhor, H. R.; Laurent, S.; Lynch, I. Protein Fibrillation and Nanoparticle Interactions: Opportunities and Challenges. *Nanoscale* **2013**, *5*, 2570–2588. 849
20. Zaman, M.; Ahmad, E.; Qadeer, A.; Rabbani, G.; Khan, R. H. Nanoparticles in Relation to Peptide and Protein Aggregation. *Int. J. Nanomed.* **2014**, *9*, 899–912. 850

- 901 21. Linse, S.; Cabaleiro-Lago, C.; Xue, W.-F.; Lynch, I.; Lindman,
902 S.; Thulin, E.; Radford, S. E.; Dawson, K. A. Nucleation of
903 Protein Fibrillation by Nanoparticles. *Proc. Natl. Acad. Sci.*
904 *U.S.A.* **2007**, *104*, 8691–8696.
- 905 22. Gejyo, F.; Yamada, T.; Odani, S.; Nakagawa, Y.; Arakawa, M.;
906 Kunitomo, T.; Kataoka, H.; Suzuki, M.; Hirasawa, Y.; Shirahama,
907 T.; et al. A New Form of Amyloid Protein Associated with
908 Hemodialysis Was Identified as β_2 -Microglobulin. *Bio-*
909 *chem. Biophys. Res. Commun.* **1985**, *129*, 701–706.
- 910 23. Relini, A.; Canale, C.; De Stefano, S.; Rolandi, R.; Giorgetti, S.;
911 Stoppini, M.; Rossi, A.; Fogolari, F.; Corazza, A.; Esposito, G.;
912 et al. Collagen Plays an Active Role in the Aggregation of
913 β_2 -Microglobulin under Physiopathological Conditions of
914 Dialysis-Related Amyloidosis. *J. Biol. Chem.* **2006**, *281*,
915 16521–16529.
- 916 24. Xia, Y.; Xiong, Y.; Lim, B.; Skrabalak, S. E. Shape-Controlled
917 Synthesis of Metal Nanocrystals: Simple Chemistry Meets
918 Complex Physics? *Angew. Chem., Int. Ed.* **2009**, *48*, 60–103.
- 919 25. Sperling, R.; Gil, P.; Zhang, F.; Zanella, M.; Parak, W. J.
920 Biological Applications of Gold Nanoparticles. *Chem. Soc.*
921 *Rev.* **2008**, *37*, 1896–1908.
- 922 26. Calzolari, L.; Franchini, F.; Gilliland, D.; Rossi, F. Protein–
923 Nanoparticle Interaction: Identification of the Gold Nano-
924 particle Interaction Site. *Nano Lett.* **2010**, *10*, 3101–3105.
- 925 27. Brancolini, G.; Kokh, D. B.; Calzolari, L.; Wade, R. C.; Corni, S.
926 Docking of Ubiquitin to Gold Nanoparticles. *ACS Nano*
927 **2012**, *6*, 9863–9878.
- 928 28. Sabella, S.; Carney, R. P.; Brunetti, V.; Malvindi, M. A.; Al-
929 Juffali, N.; Vecchio, G.; Janes, S. M.; Bakr, O. M.; Cingolani, R.;
930 Stellacci, F.; et al. A General Mechanism for Intracellular
931 Toxicity of Metal-Containing Nanoparticles. *Nanoscale*
932 **2014**, *6*, 7052–7061.
- 933 29. Park, J.-W.; Shumaker-Parry, J. S. Structural Study of Citrate
934 Layers on Gold Nanoparticles: Role of Intermolecular
935 Interactions in Stabilizing Nanoparticles. *J. Am. Chem.*
936 *Soc.* **2014**, *136*, 1907–1921.
- 937 30. Relini, A.; De Stefano, S.; Torrassa, S.; Cavalieri, O.; Rolandi,
938 R.; Gliozzi, A.; Giorgetti, S.; Raimondi, S.; Marchese, L.; Verga,
939 L.; et al. Heparin Strongly Enhances the Formation of
940 β_2 -Microglobulin Amyloid Fibrils in the Presence of Type I
941 Collagen. *J. Biol. Chem.* **2008**, *283*, 4912–4920.
- 942 31. Colvin, V. M.; Kulinowski, K. M. Nanoparticles as Catalysts
943 for Protein Fibrillation. *Proc. Natl. Acad. Sci. U.S.A.* **2007**,
944 *104*, 8679–8680.
- 945 32. Elechiguerra, J. L.; Reyes-Gasga, J.; Yacamán, M. J. The Role
946 of Twinning in Shape Evolution of Anisotropic Noble Metal
947 Nanostructures. *J. Mater. Chem.* **2006**, *16*, 3906–3919.
- 948 33. Kunze, J.; Burgess, I.; Nichols, R.; Buess-Herman, I.; Lipkowski,
949 J. Electrochemical Evaluation of Citrate Adsorption on
950 Au(111) and the Stability of Citrate-Reduced Gold Colloids.
951 *J. Electroanal. Chem.* **2007**, *599*, 147–159.
- 952 34. Vivek, J. P.; Burgess, I. J. Insight into Chloride Induced
953 Aggregation of DMAP-Monolayer Protected Gold Nano-
954 particles Using the Thermodynamics of Ideally Polarized
955 Electrodes. *J. Phys. Chem. C* **2008**, *112*, 2872–2880.
- 956 35. Scott, H.; Brewer, S. H.; Glomm, W. R.; Marcus, C.; Johnson,
957 M. C.; Magne, K.; Knag, M. K.; Franzen, S. Probing BSA
958 Binding to Citrate-Coated Gold Nanoparticles and Sur-
959 faces. *Langmuir* **2005**, *21*, 9303–9307.
- 960 36. Lin, Y.; Pan, G.-B.; Su, G.-J.; Fang, X.-H.; Wan, L.-J.; Bai, C.-L.
961 Study of Citrate Adsorbed on the Au(111) Surface by
962 Scanning Probe Microscopy. *Langmuir* **2003**, *19*, 10000–
963 10003.
- 964 37. Rostek, A.; Mahl, D.; Epple, M. Chemical Composition of
965 Surface-Functionalized Gold Nanoparticles. *J. Nanopart.*
966 *Res.* **2011**, *13*, 4809–4814.
- 967 38. Wright, L. B.; Rodgera, P. M.; Walsh, T. R. Aqueous Citrate: A
968 First-Principles and Force-Field Molecular Dynamics
969 Study. *RSC Adv.* **2013**, *3*, 16399–16409.
- 970 39. Lin, Y.; Pan, G.; Su, G.-J.; Fang, X.-H.; Wan, L.-J.; Bai, C.-L.
971 Study of Citrate Adsorbed on the Au(111) Surface by
972 Scanning Probe Microscopy. *Langmuir* **2003**, *19*, 10000–
973 10003.
- 974 40. Kokh, D. B.; Corni, S.; Winn, P. J.; Hoefling, M.; Gottschalk,
975 K. E.; Wade, R. C. ProMetCS: An Atomistic Force Field for
Modeling Protein–Metal Surface Interactions in a Con-
tinuum Aqueous Solvent. *J. Chem. Theory Comput.* **2010**,
6, 1753–1768.
41. Gabdouliline, R. R.; Wade, R. C. Effective Charges for
Macromolecules in Solvent. *J. Phys. Chem.* **1996**, *100*,
3868–3878.
42. Sugita, Y.; Okamoto, Y. Replica-Exchange Molecular
Dynamics Method for Protein Folding. *Chem. Phys. Lett.*
1999, *314*, 141–151.
43. Hansmann, U. H. E. Parallel Tempering Algorithm for
Conformational Studies of Biological Molecules. *Chem.*
Phys. Lett. **1997**, *281*, 140–150.
44. Eichner, T.; Kalverda, A. P.; Thompson, G. S.; Homans, S. W.;
Radford, S. E. Conformational Conversion during Amyloid
Formation at Atomic Resolution. *Mol. Cell* **2011**, *41*,
161–172.
45. Esposito, G.; Ricagno, S.; Corazza, A.; Rennella, E.; Gumral,
D.; Mimmi, M.; Betto, E.; Pucillo, C.; Fogolari, F.; Viglino, P.;
et al. NMR Spectroscopy Reveals Unexpected Structural
Variation at the Protein–Protein Interface in MHC Class I
Molecules. *J. Mol. Biol.* **2008**, *378*, 887–897.
46. Eichner, T.; Radford, S. E. A Generic Mechanism of β_2 -
Microglobulin Amyloid Assembly at Neutral pH Involving a
Specific Proline Switch. *J. Mol. Biol.* **2009**, *386*, 1312–1326.
47. Stober, T. S.; Abrams, F. C. Energetics and Mechanism of
the Normal-to-Amyloidogenic Isomerization of β_2 -
Microglobulin: On-the-Fly String Method Calculations.
J. Phys. Chem. B **2012**, *116*, 9371–9375.
48. Verdone, G.; Corazza, A.; Viglino, P.; Pettirossi, F.; Giorgetti,
S.; Mangione, P.; Andreola, A.; Stoppini, M.; Bellotti, V.;
Esposito, G. The Solution Structure of Human β_2 -Micro-
globulin Reveals the Prodromes of Its Amyloid Transition.
Protein Sci. **2002**, *11*, 487–499.
49. Corazza, A.; Pettirossi, F.; Viglino, P.; Verdone, G.; Garcia, J.;
Dumy, P.; Giorgetti, S.; Mangione, P.; Raimondi, S.; Stoppini,
M.; et al. Properties of Some Variants of Human β_2 -
Microglobulin and Amyloidogenesis. *J. Biol. Chem.* **2004**,
279, 9176–9189.
50. Esposito, G.; Corazza, A.; Viglino, P.; Verdone, G.; Pettirossi,
F.; Fogolari, F.; Makek, A.; Giorgetti, S.; Mangione, P.;
Stoppini, M.; et al. Solution Structure of β_2 -Microglobulin
and Insights into Fibrillogenesis. *Biochim. Biophys. Acta*
2005, *1753*, 76–84.
51. Giorgetti, S.; Rossi, A.; Mangione, P.; Raimondi, S.; Marini, S.;
Stoppini, M.; Corazza, A.; Viglino, P.; Esposito, G.; Cetta, G.;
et al. β_2 -Microglobulin Isoforms Display an Heteroge-
neous Affinity for Type I Collagen. *Protein Sci.* **2005**, *14*,
696–702.
52. Brancolini, G.; Migliore, A.; Corni, S.; Fuentes-Cabrera, M.;
Luque, F. J.; Di Felice, R. Dynamical Treatment of Charge
Transfer through Duplex Nucleic Acids Containing Mod-
ified Adenines. *ACS Nano* **2013**, *7*, 9396–9406.
53. Soliva, R.; Sherer, E.; Luque, F. J.; Laughton, C. A.; Orozco, M.
Molecular Dynamics Simulations of PNA3DNA and PNA3R-
NA Duplexes in Aqueous Solution. *J. Am. Chem. Soc.* **2000**,
122, 5997–6008.
54. Spector, T. I.; Cheatham, T. E.; Kollman, P. A. Unrestrained
Molecular Dynamics of Photodamaged DNA in Aqueous
Solution. *J. Am. Chem. Soc.* **1997**, *119*, 7095–7104.
55. Brancolini, G.; Toroz, D.; Corni, S. Can Small Hydrophobic
Gold Nanoparticles Inhibit β_2 -Microglobulin Fibrillation?
Nanoscale **2014**, *6*, 7903–7911.
56. Fogolari, F.; Corazza, A.; Varini, N.; Rotter, M.; Gumral, D.;
Codutti, L.; Rennella, E.; Viglino, P.; Bellotti, V.; Esposito, G.
Molecular Dynamics Simulations of β_2 -Microglobulin in
Denaturing and Stabilizing Conditions. *Proteins* **2011**, *79*,
986–1001.
57. Fogolari, F.; Corazza, A.; Yarra, V.; Jalaru, A.; Esposito, G.
BLUUES: A Program for the Analysis of the Electrostatic
Properties of Proteins Based on Generalized Born Radii.
BMC Bioinf. **2012**, *13*, S18.
58. Brewer, S. H.; Glomm, W. R.; Johnson, M. C.; Knag, M. K.;
Franzen, S.; Gold, D. L. M. Probing BSA Binding to Citrate-
Coated Gold Nanoparticles and Surfaces. *Langmuir* **2005**,
21, 9303–9307.

- 1051 59. Dolinsky, T. J.; Czodrowski, P.; Li, H.; Nielsen, J. E.; Jensen,
1052 J. H.; Klebe, G.; Baker, N. A. PDB2PQR: Expanding and
1053 Upgrading Automated Preparation of Biomolecular Structures
1054 for Molecular Simulations. *Nucleic Acids Res.* **2007**,
1055 *35*, W522–525.
- 1056 60. Hwang, T. L.; Shaka, A. J. Water Suppression That Works.
1057 Excitation Sculpting Using Arbitrary Waveforms and
1058 Pulsed Field Gradients. *J. Magn. Reson., Ser. A* **1995**, *112*,
1059 275–279.
- 1060 61. Johnson, B. A.; Blevins, R. A. NMR View: A Computer
1061 Program for the Visualization and Analysis of NMR Data.
1062 *J. Biomol. NMR* **1994**, *4*, 603–614.
- 1063 62. Gabdoulline, R. R.; Wade, R. C. Simulation of the Diffusional
1064 Association of Barnase and Barstar. *Biophys. J.* **1997**, *72*,
1065 1917–1929.
- 1066 63. www.h-its.org/mcm.
- 1067 64. Iori, F.; Di Felice, R.; Molinari, E.; Corni, S. GolP: An Atomistic
1068 Force-Field To Describe the Interaction of Proteins with
1069 Au(111) Surfaces in Water. *J. Comput. Chem.* **2009**, *30*,
1070 1465–1476.
- 1071 65. Esposito, G.; Corazza, A.; Bellotti, V. Pathological Self-
1072 Aggregation of β_2 -Microglobulin: A Challenge for Protein
1073 Biophysics. *Subcell. Biochem.* **2012**, *65*, 1917–1929.
- 1074 66. Baker, N. A.; Sept, D.; Joseph, S.; Holst, M. J.; McCammon,
1075 J. A. Electrostatics of Nanosystems: Application to Micro-
1076 tubules and the Ribosome. *Proc. Natl. Acad. Sci. U.S.A*
1077 **2001**, *98*, 10037–10041.
- 1078 67. Elcock, A. H.; Gabdoulline, R. R.; Wade, R. C.; McCammon,
1079 J. A. Computer Simulation of Protein–Protein Association
1080 Kinetics: Acetylcholinesterase-Fasciculin. *J. Mol. Biol.* **1999**,
1081 *291*, 149–162.
- 1082 68. <http://biophysics.cs.vt.edu/H++>.
- 1083 69. van der Spoel, D.; Lindahl, E.; Hess, B.; Groenhof, G.; Mark,
1084 A. E.; Berendsen, H. J. C. GROMACS: Fast, Flexible, and Free.
1085 *J. Comput. Chem.* **2005**, *26*, 1701–1718.
- 1086 70. Jorgensen, W. L.; Maxwell, D. S.; TiradoRives, J. Develop-
1087 ment and Testing of the OPLS All-Atom Force Field on
1088 Conformational Energetics and Properties of Organic
1089 Liquids. *J. Am. Chem. Soc.* **1996**, *118*, 11225–11236.
- 1090 71. Hess, B.; van der Vegt, N. F. Hydration Thermodynamic
1091 Properties of Amino Acid Analogues: A Systematic Compar-
1092 ison of Biomolecular Force Fields and Water Models.
1093 *J. Phys. Chem. B* **2006**, *110*, 17616–17626.

